Electronic supplementary material (ESI) for

Tuning the CO oxidation catalytic activity of supported metal-metal oxide hetero-structures by an aqueous phase post-treatment process

Chunzheng Wu[a,b], Rosaria Brescia[a], Mirko Prato[a], Sergio Marras[a], Liberato Manna[a], Massimo Colombo[a]*

a) Department of Nanochemistry, Istituto Italiano di Tecnologia, Via Morego 30, Genova, 16163, Italy.
b) Dipartimento di Chimica e Chimica Industriale, Università di Genova, via Dodecaneso 31-I-16146 Genova, Italy

massimo.colombo@iit.it (corresponding author email)

Experimental

Materials

Tetrachloroauric (III) acid hydrate (48.5-50.25 % Au, $HAuCl_4 \cdot (H_2O)_x$), tetralin (1,2,3,4-Tetrahydronaphthalene, 99 %) , borane tert-butylamine complex (TBAB, 97 %), manganese(II) chloride tetrahydrate ($MnCl_2 \cdot 4H_2O$, ≥ 99 %), oleic acid (technical grade, 90 %), 1-octadecene (technical grade, 90 %), iron(II) perchlorate tetrahydrate (99.99 %), toluene (≥ 99.7 % (GC)), chloroform (99.0-99.4 % (GC)), methanol (≥ 99.9 %), isopropanol (≥ 99.8 % (GC)), acetone (≥ 99.5 % (GC)), octadecanethiol (ODT, 98 %), tin (II) chloride dihydrate (≥ 99.99 %), cerium (III) chloride heptahydrate (99.9 %), cobalt (II) perchlorate hexahydrate, 1-octanol (≥ 99 %) were purchased from Sigma-Aldrich. Oleylamine (80-90 %) was purchased from ACROS ORGANICS. Hexane, hydrochloric acid (≥ 37 %), and ethanol were purchased from Fluka. Sodium hydroxide (pellets, NaOH, 98.0 %) was purchased from Panreac AppliChem. Hydrophilic fumed silica (AEROSIL-380) was purchased from Evonik Industries. Xylene (≥ 98.5 %) was purchased from Carlo Erba. All the chemicals were used without further purification. Ultrapure Milli-Q® (18.2 MΩ•cm) was used as water source.

Synthesis of ODT-functionalized Au NCs

Au NCs were prepared according to the method reported by Sun et al.[1] Briefly, 100 mg $HAuCl_4 \cdot H_2O$ was dissolved in a mixture of 10 ml oleylamine and 10 ml tetralin, and the solution was stirred under N_2 for 10 min at 20 °C. Then, 0.5 mmol TBAB was dissolved in a mixture of 1 ml oleylamine and 1 ml tetralin, and the mixture was injected into the Au precursor solution quickly. After stirring for 1 hour, the Au NCs were precipitated with ethanol and collected by centrifugation. The Au NCs were re-dispersed in hexane, followed by the addition of ethanol and centrifugation. The washing process was repeated twice and the final product was dispersed in 10 ml of toluene. This colloidal suspension was then mixed with 10 ml of toluene containing 3 mmol (0.86 g) of ODT.

The mixture was stirred under N_2 at room temperature overnight in order to obtain ODT functionalized Au NCs. The particles were precipitated with ethanol, and collected by centrifugation. The NCs were re-dispersed in hexane, followed by the addition of ethanol and centrifugation. The washing process was repeated twice and the final product was dispersed in hexane and stored in a fridge. The ligand exchange from oleylamine to ODT was crucial for the preparation of Au-MnO heterodimers.

Synthesis of Au-MnO heterodimers

The Au-MnO heterodimers were synthesized according to the procedure reported by Tremel et al.[2] with some modifications. Typically, in order to synthesize the 4 nm-15 nm Au-MnO NPs, a mixture of 2.0 mmol Mn(II)-oleate (prepared following the procedures reported by Tremel et al.[3]), 30 mmol oleylamine, 30 mmol oleic acid, and 100 ml 1-octadecene was degassed in N_2 at 80 ^{o}C for 1 hour. Then a hexane solution of ODT-functionalized Au NCs (which contains 20 mg of Au) was added to the mixture and further degassed for 30 min to remove the hexane. After that, the mixture was heated up to 315 ^{o}C with a rate of 2 ^{o}C/min under a vigorous N_2 flow. After approaching 315 ^{o}C, the N_2 flow was reduced and the reaction was held at reflux for 90 min before cooling down to room temperature. The particles were precipitated with acetone and collected by centrifugation. The product was re-dispersed in hexane, followed by the addition of isopropanol and centrifugation. The final product was dispersed in hexane and stored in a fridge.

Preparation of Au-Mn$_3$O$_4$/SiO$_2$, Au/SiO$_2$, Mn$_3$O$_4$/SiO$_2$ and Co$_3$O$_4$/SiO$_2$ samples

A colloidal deposition method was used to prepare the silica supported samples. For the Au-Mn$_3$O$_4$/SiO$_2$ sample, 2200 mg of fumed SiO$_2$ were dispersed in 600 ml of hexane. Then, a hexane solution of Au-MnO (targeting 1 wt. % of Au) was added to the mixture dropwise under stirring. The mixture was then sonicated for 30 min to improve the NCs dispersion. The products were collected by centrifugation and dried at 60 ^{o}C overnight. To remove the ligands and oxidize the MnO domains to Mn$_3$O$_4$, the sample was calcined at 450 ^{o}C for 3 hours in a muffle furnace.

Oleylamine functionalized Au NCs synthesized according to the procedure described above were used for the preparation of the Au/SiO$_2$ catalyst. MnO NCs prepared according to Tremel et al.[3] were used for the preparation of the Mn$_3$O$_4$/SiO$_2$ catalyst. The Au/SiO$_2$ and the Mn$_3$O$_4$/SiO$_2$ samples were prepared with the same mass load of Au and Mn of the Au-Mn$_3$O$_4$/SiO$_2$ sample. The deposition and calcination procedures for Au/SiO$_2$ and Mn$_3$O$_4$/SiO$_2$ were the same adopted for the Au-Mn$_3$O$_4$/SiO$_2$ sample. Co$_3$O$_4$ nanocubes (prepared by a hydrothermal method[4]) were dispersed in xylene and deposited on SiO$_2$ via colloidal deposition, followed by calcination.

Post-treatment procedure

Aliquots of 300 mg of the Au-Mn$_3$O$_4$/SiO$_2$ were dispersed in 150 ml of H$_2$O with sonication. The mixture was heated up to 90 ^{o}C within 15 min under stirring and 15 ml of Fe(ClO$_4$)$_2$ aqueous solution was injected into the mixture quickly. The concentration of the Fe(ClO$_4$)$_2$ solution was varied in the range 1.67-333.33 mM in order to prepare different products. After reacting for 90 min at 90 ^{o}C, the product was collected by centrifugation, washed twice with H$_2$O and washed once with ethanol. Finally, the sample was dried at 60 ^{o}C overnight. The post-treatment was performed in air, unless specifically mentioned. The post-treated samples were named as Au-MnO$_x$/SiO$_2$-PT1 to PT5, while the starting sample was named as Au-MnO$_x$/SiO$_2$-NonPT. The same post-treatment procedure was performed over the Au/SiO$_2$ and Mn$_3$O$_4$/SiO$_2$ samples in order to perform control experiments.

The same experimental conditions were used for the Ce^{3+} and Sn^{2+} post-treatment on Mn$_3$O$_4$/SiO$_2$ and for the Sn^{2+} post-treatment on Co$_3$O$_4$/SiO$_2$. To this aim the Fe(ClO$_4$)$_2$ solution was simply replaced by a CeCl$_3$ aqueous solution or a SnCl$_2$/HCl aqueous solution respectively (HCl was used to prevent the precipitation of Sn species).

Material characterization

For transmission electron microscopy (TEM) analyses, 10 mg of the catalyst powder samples were suspended in 1 mL of ethanol and mildly sonicated. About 100 μL of the supernatant was then

deposited onto ultrathin carbon-coated Cu grids. For the as-synthesized Au-MnO samples, 100 μL of the suspension was deposited onto carbon-coated grids. Overview bright-field (BF) TEM images were recorded using a JEOL JEM-1011 instrument with a thermionic W source operated at 100 kV. The high resolution TEM (HRTEM) images were recorded using an image C_s-corrected JEOL JEM-2200FS TEM with a Schottky emitter, operated at 200 kV. EDS analyses were carried out in scanning TEM (STEM) mode using the same microscope, equipped with a Quantax 400 STEM system and a XFlash 5060 silicon-drift detector (SDD, 60 mm^2 active area). The reported EDS maps were obtained by integrating the Au Lα, Mn Kα, Fe Kα and Si Kα peaks in the spectra. Tilt series of high-angle annular dark field (HAADF)-STEM images were acquired using a FEI Tecnai G2 F20 instrument with a Schottky emitter operated at 200 kV acceleration voltage. The X-Ray Diffraction (XRD) measurements were performed using a PANalytical Empyrean X-Ray diffractometer equipped with a 1.8kW Cu Kα ceramic X-ray tube, PIXcel3D 2x2 area detector and operating at 45 kV and 40 mA. The diffraction patterns were collected in Parallel-Beam (PB) geometry and symmetric reflection mode using a zero-diffraction silicon substrate. XRD data analysis was carried out using HighScore 4.1 software from PANalytical. X-ray photoelectron spectroscopy (XPS) characterizations were performed to get insights on the oxidation states of the elements in the hetero-dimers. All the measurements have been performed on a Kratos Axis Ultra[DLD] spectrometer using a monochromatic Al Kα source (15kV, 20mA). The binding energy was calibrated by setting the main C 1s peak (corresponding to C-C bonds) to 284.8 eV. The chemical composition of the catalysts were measured by Inductively Coupled Plasma Optical Emission Spectroscopy (ICP-OES) using a iCAP 6000 Thermo Scientific spectrometer. A specific weight of catalyst was digested in HCl/HNO$_3$ 3:1 (v/v) overnight, diluted with Milli-Q®water and filtered using a PTFE filter before measurement. The thermogravimetric analysis (TGA) was performed using a TGA Q500 instrument, from room temperature to 600 °C with a heating rate of 5 °C/min in air flux.

Catalytic tests

The CO oxidation catalytic activity was measured using a micro reactor system coupled with a NDIR analyzer that allowed the continuous detection of CO and CO_2 concentrations at the reactor outlet. Typically, 80 mg of catalyst powder was loaded into a quartz reactor (internal diameter = 4 mm). The feed gas was a mixture of 1 % v/v CO and 6 % v/v O_2 balanced with He. The flow rate was set in order to have a gas hourly space velocity of 6 x 10^4 $Nml/h/g_{cat.}$. The catalysts were tested directly without any pretreatment (i.e. for the $Au-Mn_3O_4/SiO_2$ catalyst, the test was performed after calcination in muffle furnace, while for the post-treated catalysts, the tests were performed after the drying step at 60 °C). For one test cycle, the reactor was heated from room temperature to 280 °C with a heating rate of 5 °C/min and kept at 280 °C for 30 min, then cooled down to RT. To ensure that the obtained activity results were reliable, the test cycle for each catalyst was repeated 4 times. Transient activity data were collected during the test, and the CO conversion was defined as the percentage of CO feed that had reacted.

Temperature programmed reduction (TPR):

TPR measurements were performed on ~70 mg of the catalyst unloaded from the reactor using a Quantachrome Autosorb iQ equipped with a VICI® micro thermal conductivity detector (TCD). The $Au-MnO_x/SiO_2$-PT as well as the MnO_x/SiO_2-PT catalysts were loaded into a quartz U-tube (ID = 12 mm) and exposed to a mixture of 5 % v/v O_2 in He at 400 °C for 1 h. Then the tube was cooled down in He and, after stabilizing the temperature to 40 °C, the gas flow was switched to a mixture of 5 % v/v H_2 in Ar. The system was heated up to 900 °C at a rate of 20 °C/min while the TCD signal was being monitored.

Movie IS1: Aligned tilt series of HAADF-STEM images on the initial heterostructures, collected from -72° to +60°. in steps of 2° at high angles and 5° from -30° to +30°. The full frame size is 163.84 nm and the rotation axis is vertical and centered in the image.

Movie IS2: Aligned tilt series of HAADF-STEM images on the sample PT-1, collected from -72° to +70°. in steps of 1° at high angles and 2° from -40° to +40°. The full frame size is 225.28 nm and the rotation axis is vertical and centered in the image.

Characterization of the Au-MnO$_x$/SiO$_2$-PT:
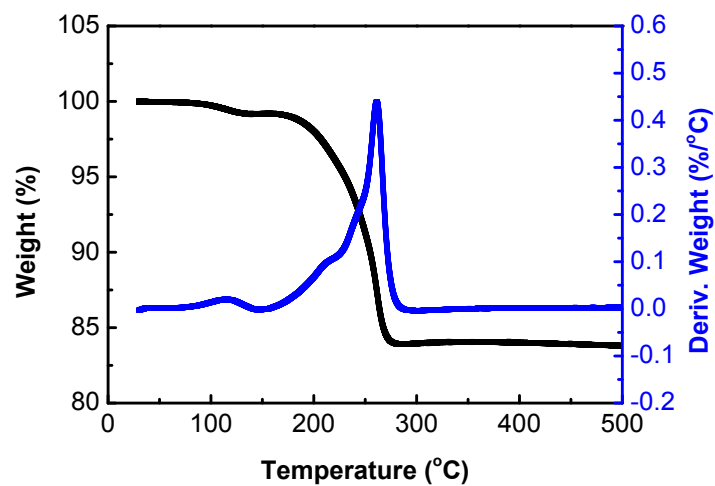
Fig.S1. TGA analysis of the Au-MnO NCs.
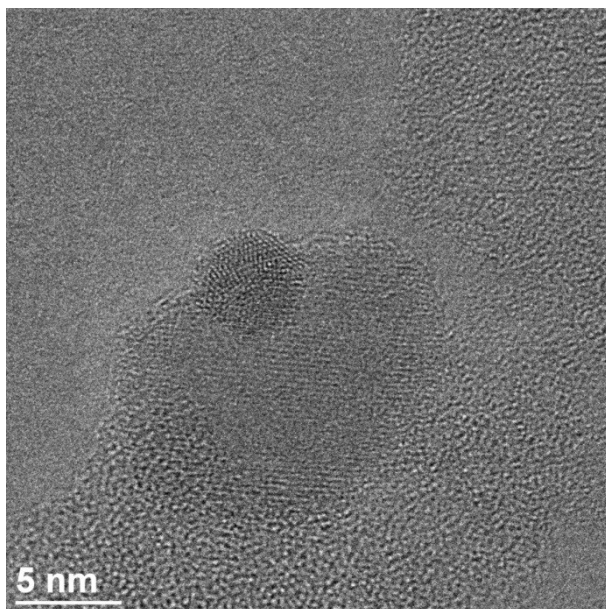
Fig. S2. HRTEM image of Au-Mn$_3$O$_4$/SiO$_2$ catalyst, clearly showing the dumbbell morphology.
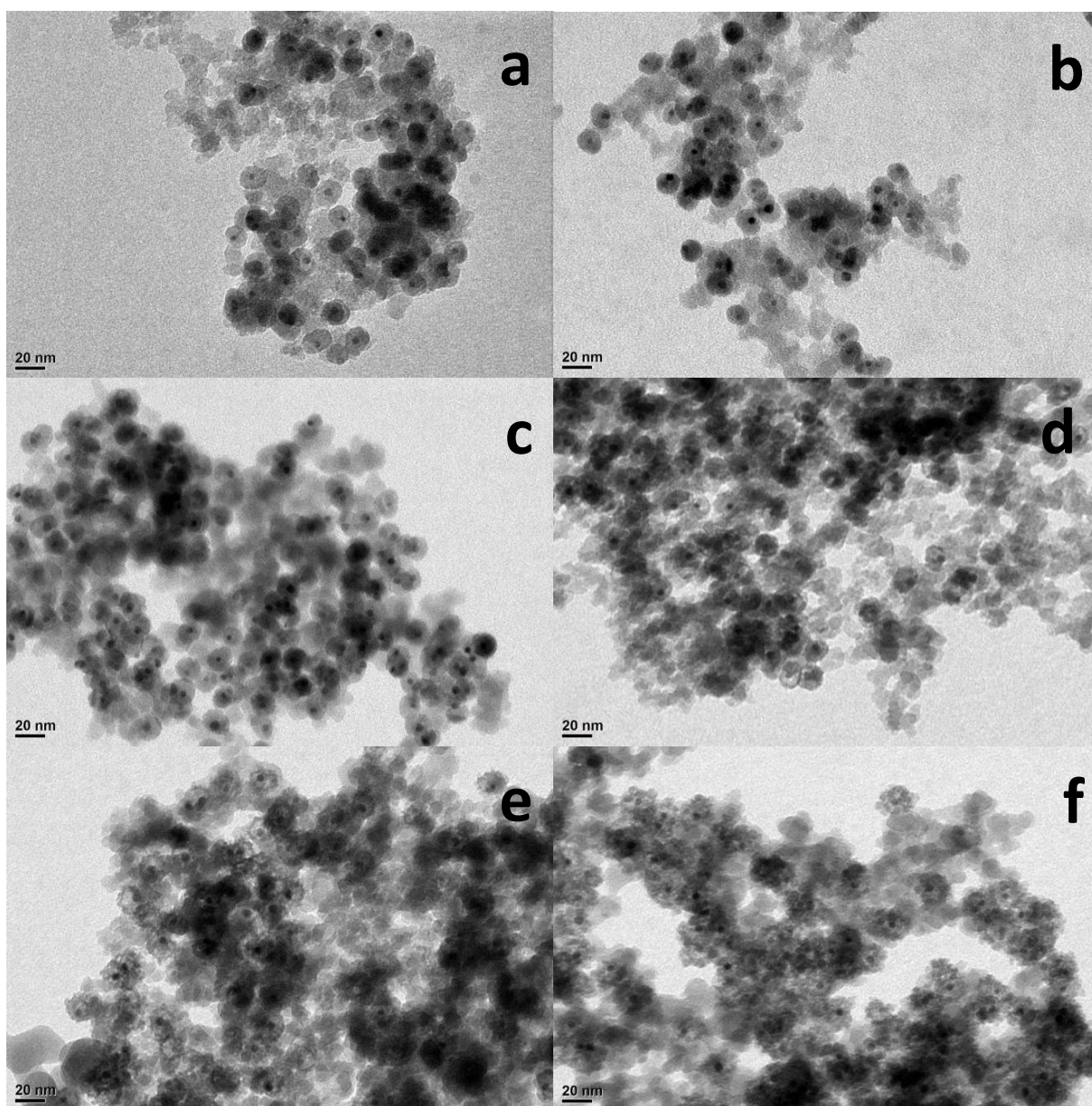
Fig.S3. Overview BF-TEM images of (a) Au-MnO$_x$/SiO$_2$-NonPT, (b) Au-MnO$_x$/SiO$_2$-PT5, (c) Au-MnO$_x$/SiO$_2$-PT4, (d) Au-MnO$_x$/SiO$_2$-PT3, (e) Au-MnO$_x$/SiO$_2$-PT2, (f) Au-MnO$_x$/SiO$_2$-PT1 samples.

For the Au-MnO$_x$/SiO$_2$-PT5 sample (Fig. S3b), with a Fe/(Fe+Mn) molar ratio of 6.8 %, the Mn$_3$O$_4$ domains showed no porosity, which meant the reaction between Mn$_3$O$_4$ and Fe(ClO$_4$)$_2$ only took place on the Mn$_3$O$_4$ surface. When the Fe/(Fe+Mn) ratio was increased to 30.9 % (Fig.S3d, Au-MnO$_x$/SiO$_2$-PT3), the reaction resulted in a significant number of semi-hollow structures. In the case of Au-MnO$_x$/SiO$_2$-PT2 (Fig.S3e) which had 67.9 % of Fe/(Fe+Mn) molar ratio, the oxide domains were definitely hollow. The difference between the Au-MnO$_x$/SiO$_2$-PT2 and the Au-MnO$_x$/SiO$_2$-PT1 samples, judging from the TEM results, was that the latter one had thicker, rougher, and more porous oxide shells than the former one. Noteworthy, for all of these treated samples, each Au NP was still associated to a single oxide domain.
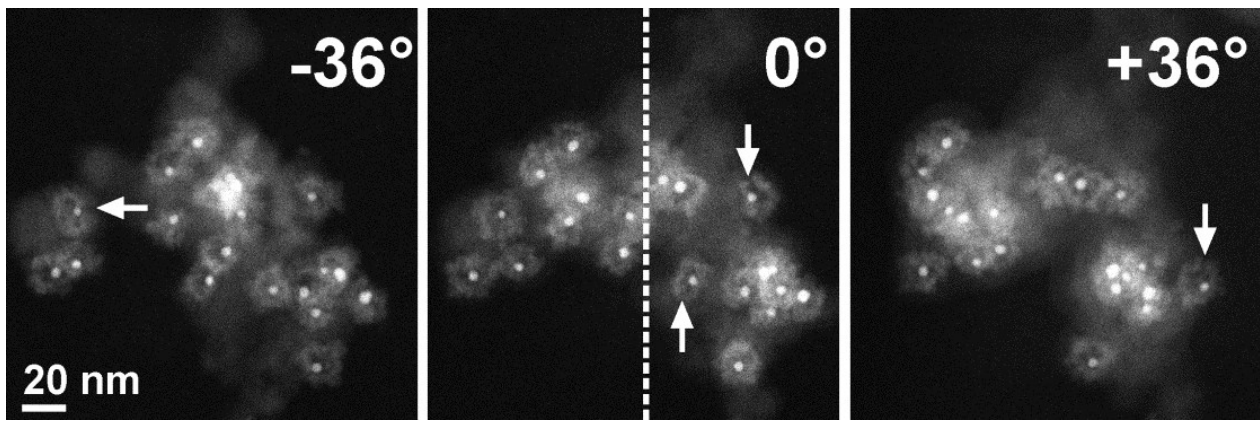
Fig.S4. HAADF-STEM images extracted from the tilted series of the Au-MnO$_x$/SiO$_2$-PT1 (movie IS1). The dashed line indicates the position of the tilt axis, while the arrows point to pinholes through the whole oxide shell.

The generality of the post-treatment procedure:

The post-treatment procedure was further extended to other metal oxide/metal cation pairs based on their reduction potentials. Considering that the standard reduction potential of the Mn_3O_4/Mn^{2+} pair is 1.82 V, we selected Ce^{3+} (Ce^{4+}/Ce^{3+} standard reduction potential of 1.72 V) and Sn^{2+} (Sn^{4+}/Sn^{2+} standard reduction potential of 0.14 V) to post-treat the Mn_3O_4/SiO_2 sample. Furthermore we exploited the post-treatment procedure starting from a different metal oxide, namely a Co_3O_4/SiO_2 sample (Co_3O_4/Co^{2+} standard reduction potential of 1.30 V), which was reacted with an aqueous Sn^{2+} solution.

Based on the TEM, XRD and ICP results reported in Fig.S5-S6 and Table. S1-2, the post-treatment was effective between the Mn_3O_4/Ce^{3+}, Mn_3O_4/Sn^{2+} and Co_3O_4/Sn^{2+} pairs. Changing either the reacting cation or the starting oxide affected both the efficiency of the replacement and the morphology of the products, which were different from those of the Mn_3O_4/Fe^{2+} pair. The low degree of replacement between Mn_3O_4 and Ce^{3+} is proposed to be related to the small reduction potential gap between the Mn_3O_4/Mn^{2+} (1.82 V) and Ce^{4+}/Ce^{3+} (1.72 V) pairs.
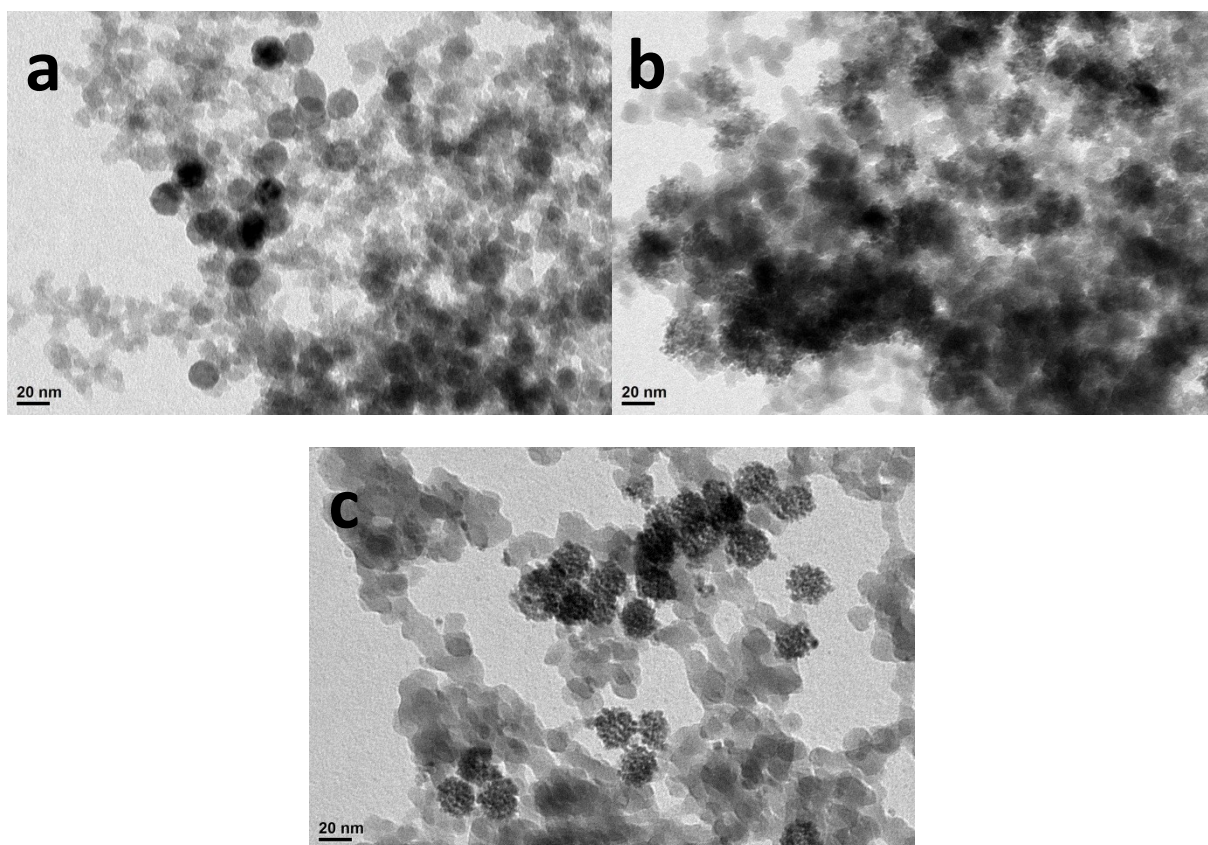
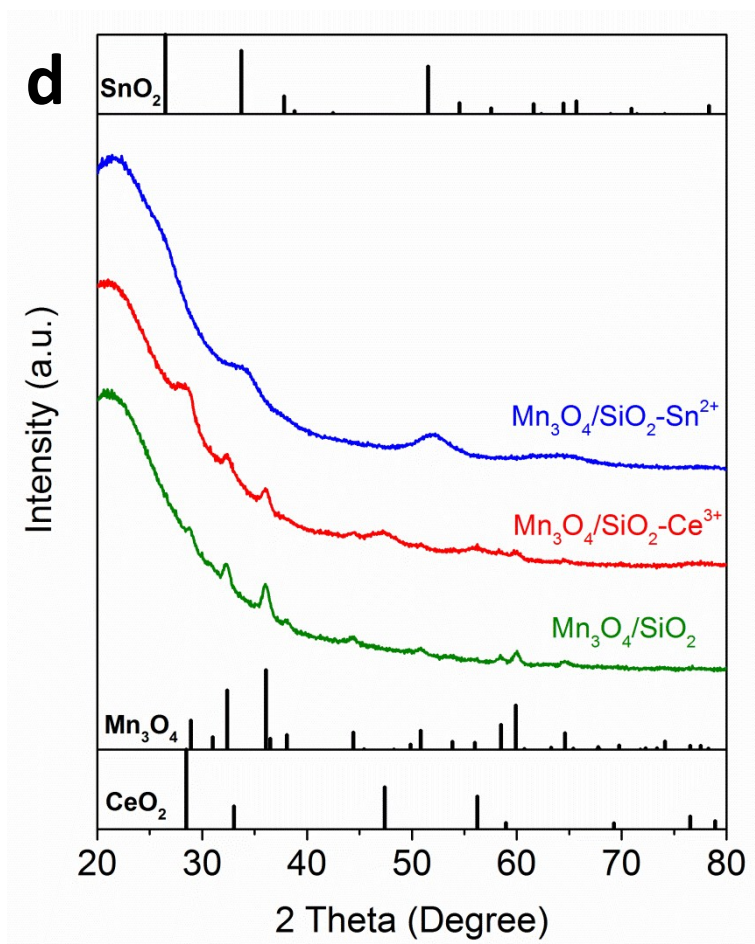Fig.S5. The BF-TEM images of (a) Mn_3O_4/SiO_2, (b) Ce^{3+} post-treated Mn_3O_4/SiO_2, and (c) Sn^{2+} post-treated Mn_3O_4/SiO_2; (d) the XRD patterns of the Mn_3O_4/SiO_2 before and after Ce^{3+} or Sn^{2+} post-treatment compared with the data base powder XRD pattern for Mn_3O_4 (ICSD: 68174), CeO_2 (ICSD: 169030), and SnO_2 (ICSD: 56671). A partial replacement with Ce^{3+} and a close to complete replacement with Sn^{2+} were observed.

Table. S1: ICP results of the Mn_3O_4/SiO_2 before and after Ce^{3+}/Sn^{2+} post-treatment.

	Ce^{3+}/Sn^{2+} added (mmol/20 mg)	HCl (ml)	Mn (wt.%)	Ce or Sn (wt.%)	$M_{Ce\ or\ Sn}/(M_{Ce\ or\ Sn}+M_{Mn})$ (at.%)
Mn_3O_4/SiO_2	-	-	2.41	-	-
Mn_3O_4/SiO_2-Ce^{3+}	≈ 0.5 (5700 %)* $CeCl_3$	-	1.41	1.10 (Ce)	23.5
Mn_3O_4/SiO_2-Sn^{2+}	0.005 (114 %)* $SnCl_2$	0.1	0	0.76 (Sn)	100

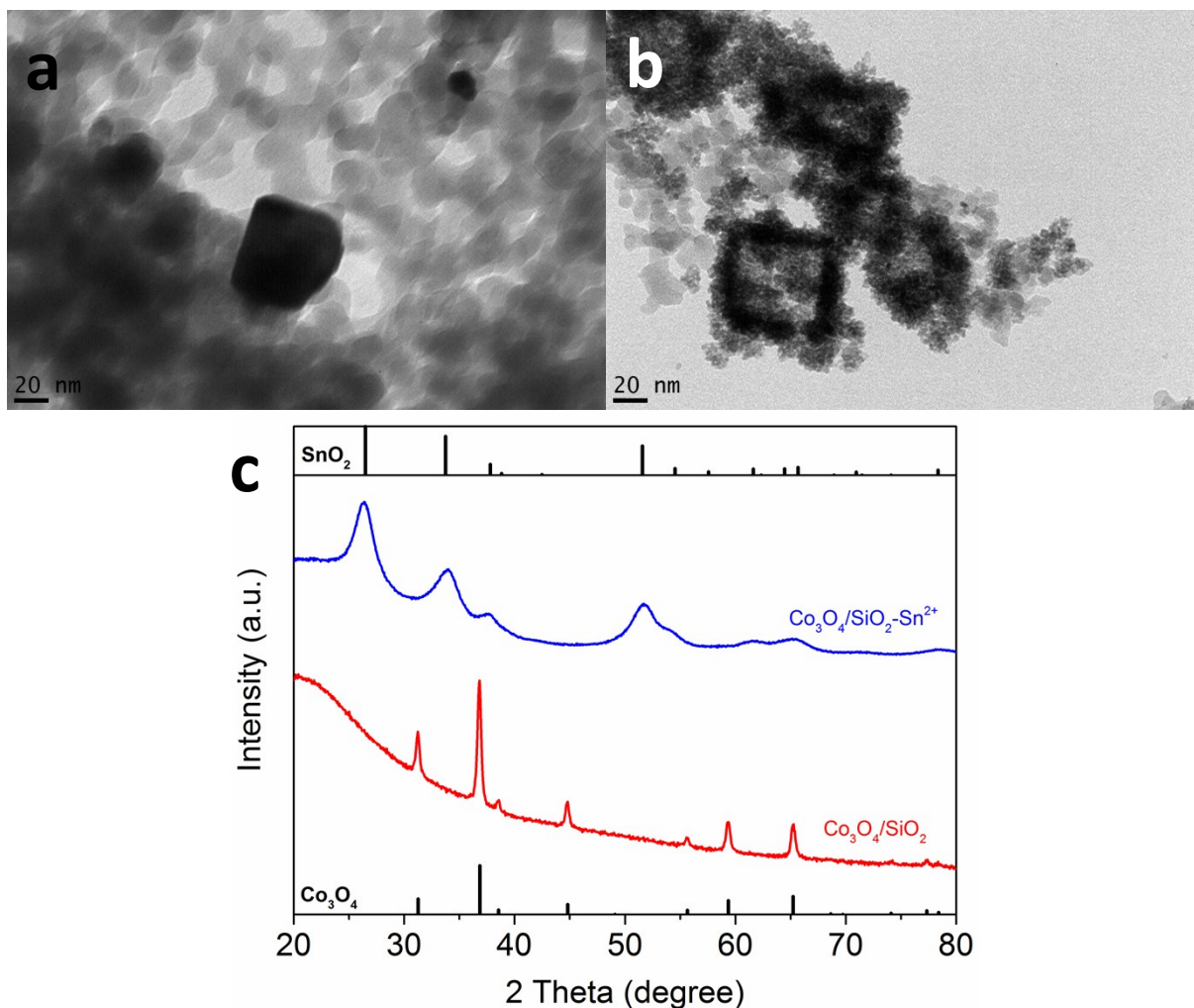* indicate the percentages of Ce^{3+} or Sn^{2+} amount added related to the stoichiometric amount of Mn.

Fig.S6, The BF-TEM images of (a) Co_3O_4/SiO_2, and (b) Sn^{2+} post-treated Co_3O_4/SiO_2; (c) XRD patterns of the Co_3O_4/SiO_2 before and after Sn^{2+} post-treatment compared with the data base powder XRD pattern for Co_3O_4 (ICSD: 24210) and SnO_2 (ICSD: 56671).

Table. S2: ICP results of the Co_3O_4/SiO_2 before and after Sn^{2+} post-treatment.

	Sn^{2+} added (mmol/20 mg)	HCl (ml)	Co (wt.%)	Sn (wt.%)	Sn/(Sn+Co) molar ratio (%)
Co_3O_4/SiO_2	-	-	8.48	-	-
Co_3O_4/SiO_2-Sn^{2+}	0.066 (230 %)* $SnCl_2$	0.2	0.04	10.74	99.3

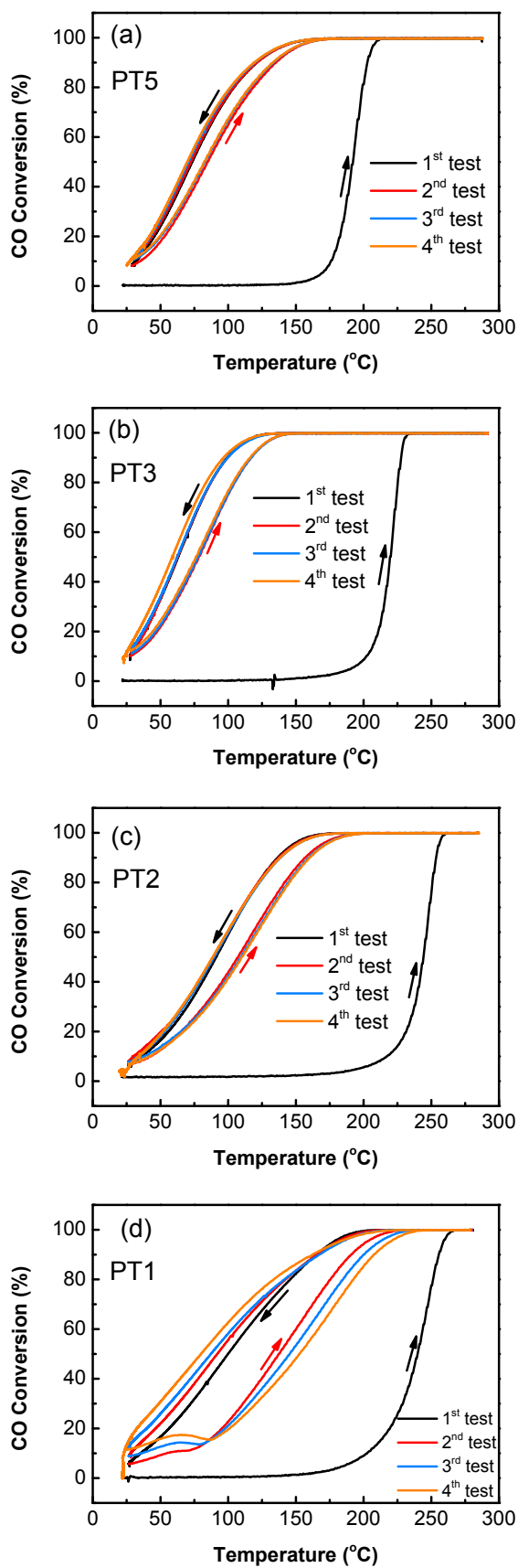* indicate the percentages of Sn^{2+} amount added related to the stoichiometric amount of Co.

CO oxidation:

Fig.S7. Relationships between temperature and CO conversion for (a) Au-MnO$_x$/SiO$_2$-PT5, (b) Au-MnO$_x$/SiO$_2$-PT3, (c) Au-MnO$_x$/SiO$_2$-PT2, (d) Au-MnO$_x$/SiO$_2$-PT1;

XPS analysis:

Table.S3: the atomic ratios of Au, Mn and Fe in the Au-MnO$_x$/SiO$_2$-PT samples obtained from XPS measurement.

	Au at.%	Mn at.%	Fe at.%
Au-MnO$_x$/SiO$_2$-NonPT	3.2	96.8	0
Au-MnO$_x$/SiO$_2$-PT4	3.8	74.7	21.5
Au-MnO$_x$/SiO$_2$-PT2	3.3	22.3	74.4
Au-MnO$_x$/SiO$_2$-PT1	1.2	0	98.8

Table.S4: the contents of different elements in Au-MnO$_x$/SiO$_2$-PT4 obtained from XPS.

	Au at.%	Mn at.%	Fe at.%	Fe/(Fe+Mn) at.%
Au-MnO$_x$/SiO$_2$-PT4 fresh	3.8	74.7	21.5	22.3
Au-MnO$_x$/SiO$_2$-PT4 tested	3.6	78.2	18.2	18.9

In order to obtain the atomic ratios between Fe, Mn and Au (as reported in table S3 and S4), XPS quantitative analysis has been performed, as described in the following. XPS peaks area can be related to the relative amount of the species which the peaks are referring to, after normalization to the so-called relative sensitivity factors – RSF (parameters that are related to the cross-section for the X-ray induced photoemission processes). Peak areas have been defined by applying a Shirley type background across the binding energy range of the peaks of interest, namely Fe 2p$_{3/2}$ (grey area in the left panel, RSF=1.971) for the quantification of Fe, Mn 2p3/2 (grey area in the middle panel, RSF =1.773) for the quantification of Mn, and Au 4f peaks (grey area in the right panel, RSF = 6.25) for the quantification of Au. Due to overlapping with Mn 3s peaks, the Au 4f peaks area has been determined through a decomposition process, bearing in mind that Mn is present as both Mn(II) and Mn(III). In this respect, Mn 3s multiplet splitting[5] has been taken into account: a splitting of 5.5 eV was considered for fitting the Mn(II) component, while a splitting of 6.5 eV was used for the Mn(III) component. In the same energy region, Fe 3s peak is present as well, as shown in Fig.S8.
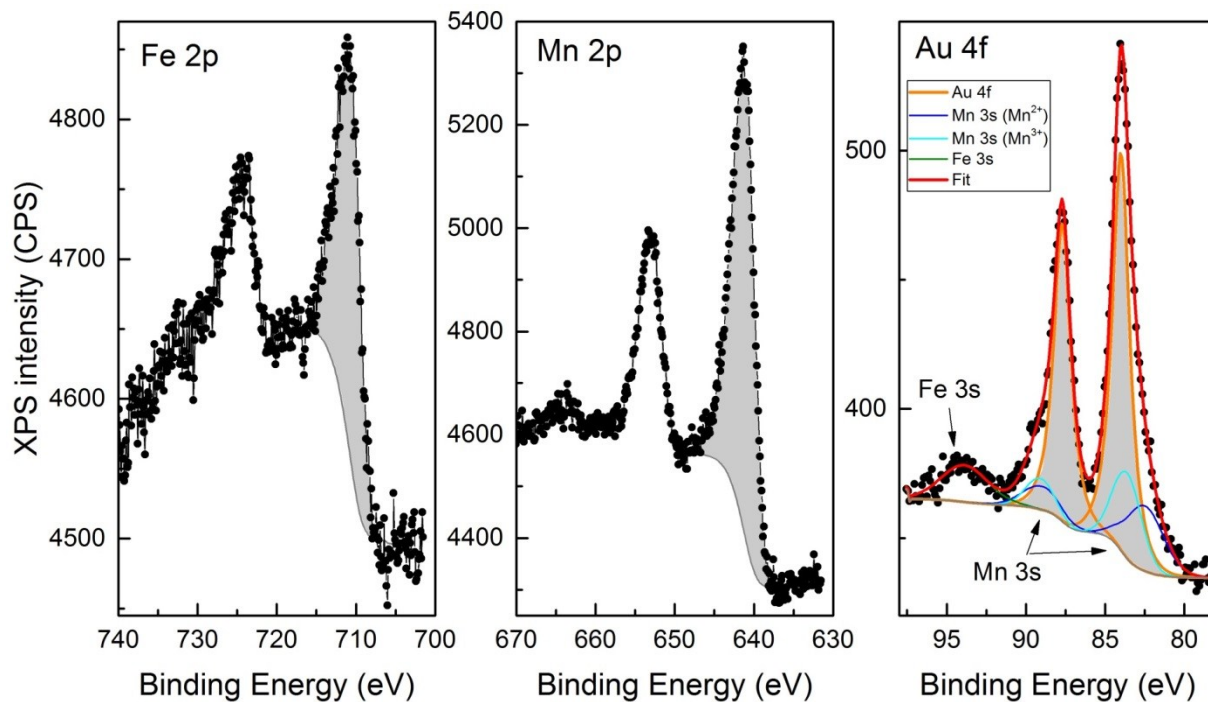
Fig.S8. XPS data collected on sample Au-MnO$_x$/SiO$_2$-PT4 over the energy regions typical for: Fe 2p (left panel), Mn 2p (middle panel), Au 4f (right panel) peaks. The data are shown to present the typical quantification protocol used over the whole set of samples.
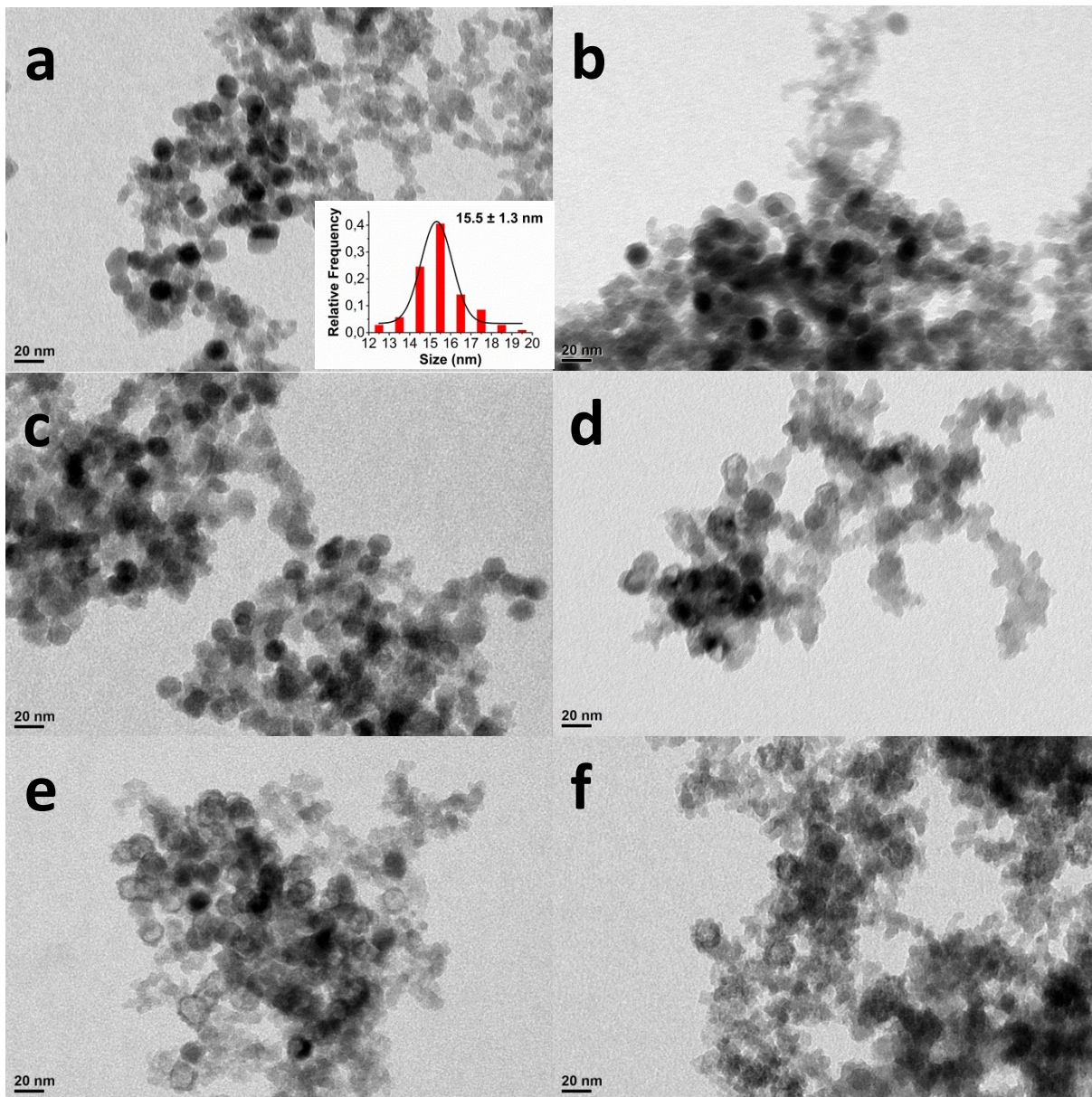
MnO$_x$/SiO$_2$-PT:

Fig.S9. Overview BF-TEM images of the MnO$_x$/SiO$_2$-PT catalysts: (a) MnO$_x$/SiO$_2$-NonPT, (inset) the size distribution of Mn$_3$O$_4$ NPs (the mean sizes was statistically evaluated by graphical measurement of more than 100 NCs), (b) MnO$_x$/SiO$_2$-PT5, (c) MnO$_x$/SiO$_2$-PT4, (d) MnO$_x$/SiO$_2$-PT3, (e) MnO$_x$/SiO$_2$-PT2, (f) MnO$_x$/SiO$_2$-PT1.

Table. S5: ICP results of the MnO_x/SiO_2-PT samples.

	Fe^{2+} amount (mmol)	Mn (wt.%)	Fe (wt.%)	Fe+Mn (mmol)	Fe/(Fe+Mn) molar ratio (%)
MnO_x/SiO_2-NonPT	0	2.93	0	0.160	**0**
MnO_x/SiO_2-PT5	0.0177 (11.1 %)[*]	3.08	0.22	0.180	**6.6**
MnO_x/SiO_2-PT4	0.0353 (22.1 %)[*]	2.70	0.52	0.175	**15.9**
MnO_x/SiO_2-PT3	0.0705 (44.1 %)[*]	1.82	1.04	0.155	**35.9**
MnO_x/SiO_2-PT2	0.129 (80.6 %)[*]	1.46	2.21	0.199	**59.8**
MnO_x/SiO_2-PT1	5 (3125 %)[*]	0.04	4.27	0.232	**99.1**

[*] indicate the percentage ratio between the moles of Fe^{2+} added and the moles of Mn in the starting catalyst.
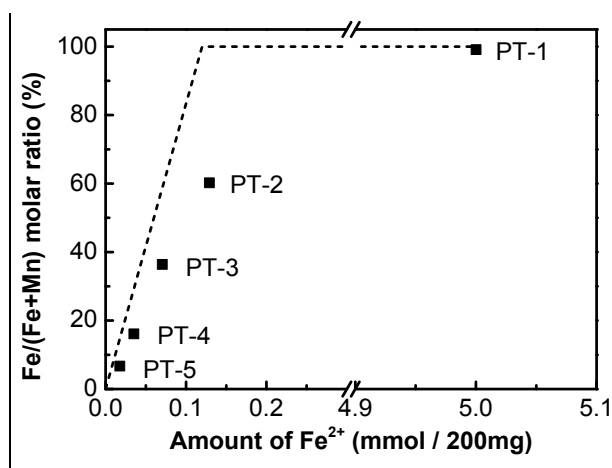

Fig.S10. Symbols: measured Fe/(Fe+Mn) molar ratio in the MnO_x/SiO_2-PT samples as a function of the Fe^{2+} amount added during the post-treatment. Dash line: Fe/(Fe+Mn) molar ratio calculated based on complete reaction of Fe^{2+}.
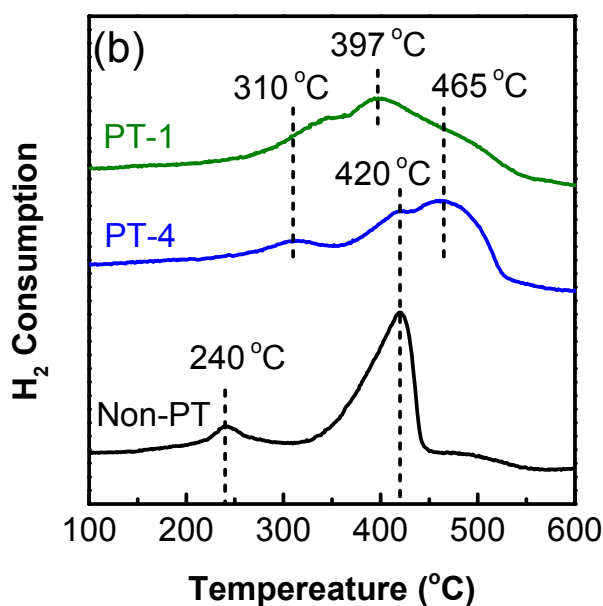
H$_2$-Temperature Programmed Reduction results:

Fig.S11. H$_2$-Temperature-programmed reduction of Mn$_3$O$_4$/SiO$_2$, MnO$_x$/SiO$_2$-PT1 and MnO$_x$/SiO$_2$-PT4 catalysts

For the starting Mn$_3$O$_4$/SiO$_2$ catalyst (Black curve), two reduction peaks were detected at around 240 °C and 420 °C. The latter one was ascribed to the reduction of Mn$_3$O$_4$ to MnO.[6, 7] The low temperature reduction peak at 240 °C indicated that a small fraction of tetrahedral Mn(II) in Mn$_3$O$_4$ were oxidized to Mn(III) during the preparation.[6, 7] To maintain the electrovalent balance, supra-stoichiometric oxygen was proposed to be bound to the tetrahedral Mn(III). The higher reducibility as well as the presence of this stoichiometric oxygen might be related to the high activity of the Mn$_3$O$_4$/SiO$_2$ sample. In the post-treated samples (i.e. PT4 and PT1), the low temperature reduction peak at 240 °C was absent; meanwhile, the reduction peak at 420 °C reduced with the deepening of the reaction, and was overlapped with the raised peaks between 300 °C and 500 °C. The overlapped peaks at around 310 °C, 397 °C and 465 °C were roughly ascribed to the reduction of Fe$_2$O$_3$ to Fe$_3$O$_4$, but we could also not exclude the possibility of the reduction from Fe$_3$O$_4$ to FeO.[8, 9] The complexity might be related to the complicated morphology, composition and crystal phase we obtained. Despite this uncertainty, it could be concluded that performing the post-treatment resulted in poorer reducibility, which was consistent with the reduced CO oxidation activity shown in Fig.6 (inset).

1.   Peng, S.; Lee, Y.; Wang, C.; Yin, H.; Dai, S.; Sun, S. A Facile Synthesis of Monodisperse Au Nanoparticles and Their Catalysis of CO Oxidation. *Nano Research* **2008,** *1*, 229-234.
2.   Schick, I.; Lorenz, S.; Gehrig, D.; Schilmann, A.-M.; Bauer, H.; Panthoefer, M.; Fischer, K.; Strand, D.; Laquai, F.; Tremel, W. Multifunctional Two-Photon Active Silica-Coated Au@MnO Janus Particles for Selective Dual Functionalization and Imaging. *Journal of the American Chemical Society* **2014,** *136*, 2473-2483.
3.   Schladt, T. D.; Graf, T.; Tremel, W. Synthesis and Characterization of Monodisperse Manganese Oxide Nanoparticles-Evaluation of the Nucleation and Growth Mechanism. *Chemistry of Materials* **2009,** *21*, 3183-3190.

4.   Oh, M. H.; Yu, T.; Yu, S.-H.; Lim, B.; Ko, K.-T.; Willinger, M.-G.; Seo, D.-H.; Kim, B. H.; Cho, M. G.; Park, J.-H.; Kang, K.; Sung, Y.-E.; Pinna, N.; Hyeon, T. Galvanic Replacement Reactions in Metal Oxide Nanocrystals. *Science* **2013,** *340*, 964-968.

5.   Ilton, E. S.; Post, J. E.; Heaney, P. J.; Ling, F. T.; Kerisit, S. N. XPS determination of Mn oxidation states in Mn (hydr)oxides. *Applied Surface Science* **2016,** *366*, 475-485.

6.   Wang, W. M.; Yang, Y. N.; Zhang, J. Y. Selective reduction of nitrobenzene to nitrosobenzene over different kinds of trimanganese tetroxide catalysts. *Applied Catalysis a-General* **1995,** *133*, 81-93.

7.   Yang, Y. N.; Huang, R. L.; Chen, L.; Zhang, J. Y. REDOX BEHAVIOR OF TRIMANGANESE TETROXIDE CATALYSTS. *Applied Catalysis a-General* **1993,** *101*, 233-252.

8.   Reddy, G. K.; Gunasekara, K.; Boolchand, P.; Smirniotis, P. G. Cr- and Ce-Doped Ferrite Catalysts for the High Temperature Water-Gas Shift Reaction: TPR and Mossbauer Spectroscopic Study. *Journal of Physical Chemistry C* **2011,** *115*, 920-930.

9.   Mou, X.; Wei, X.; Li, Y.; Shen, W. Tuning crystal-phase and shape of Fe_2O_3 nanoparticles for catalytic applications. *Crystengcomm* **2012,** *14*, 5107-5120.